

High densification of BaZrS₃ powder inspired by the cold-sintering process

Cite this Accepted Manuscript (AM) as Accepted Manuscript (AM) version of Stephen Filippone, Samuel Song, R. Jaramillo, High densification of BaZrS₃ powder inspired by the cold-sintering process, Journal of Materials Research <https://doi.org/10.1557/s43578-021-00404-1>

This AM is a PDF file of the manuscript accepted for publication after peer review, when applicable, but does not reflect post-acceptance improvements, or any corrections. Use of this AM is subject to the publisher's embargo period and AM terms of use. Under no circumstances may this AM be shared or distributed under a Creative Commons or other form of open access license, nor may it be reformatted or enhanced, whether by the Author or third parties. See here for Springer Nature's terms of use for AM versions of subscription articles: <https://www.springernature.com/gp/open-research/policies/accepted-manuscript-terms>

The Version of Record of this article, as published and maintained by the publisher, is available online at: <https://doi.org/10.1557/s43578-021-00404-1>. The Version of Record is the version of the article after copy-editing and typesetting, and connected to open research data, open protocols, and open code where available. Any supplementary information can be found on the journal website, connected to the Version of Record.

Title: High densification of BaZrS₃ powder inspired by the cold sintering process

Authors: Stephen Filippone, Samuel Song, R. Jaramillo

Department of Materials Science and Engineering, Massachusetts Institute of Technology, Cambridge, MA 02139, USA

Abstract

We report on the sintering of powders of the chalcogenide perovskite BaZrS₃ at low and intermediate temperatures. BaZrS₃ is the most widely-studied chalcogenide perovskite semiconductor. Most experimental results to-date have been made using loose powder and cold-pressed pellets (*i.e.* green bodies). Straightforward sintering methods to achieve dense ceramics are challenging because BaZrS₃ decomposes and oxidizes in air above 550°C. Here we take inspiration from the cold sintering process to develop a low-to-intermediate densification process for chalcogenide perovskites. Typical additives for cold sintering of oxides do not accelerate BaZrS₃ sintering. At higher temperature, iodine is remarkably successful as an additive to accelerate densification. We achieve density up to 92% for sintering at 450 °C and 425 MPa. Our sintering process does not cause significant oxidation. Thermogravimetric measurements reveal the formation of an intergranular phase. Impedance spectroscopy measurements reveal that the bulk dielectric properties are unaffected by ball milling and subsequent sintering.

Keywords: perovskites; sintering; thermogravimetric analysis; powder processing; dielectric properties

Introduction

Chalcogenide perovskites are an emerging class of inorganic semiconductors which combine strong visible light absorption with highly polarizable crystal structures.[1–4] In 2015, predictions of chalcogenide perovskite optical and electronic properties sparked interest in these materials for photovoltaic applications.[5] In the context of photovoltaics, chalcogenide perovskites offer a potential non-toxic, stable alternative to lead-halide perovskites. BaZrS₃ is the most well-studied chalcogenide perovskite, and is the only material for which thin films have been demonstrated.[4,6–13] BaZrS₃ forms in the orthorhombic, GdFeO₃-type, distorted-perovskite crystal structure with the space group *Pnma* (No. 62). It has a direct band gap of $E_g = 1.8$ eV with strong optical absorption above the band gap.[3,4,14]

There remains much to be learned about processing chalcogenide perovskite ceramics, *i.e.* dense polycrystalline bulk samples (the same may be said of sulfides generally).[15,16] Since chalcogenide perovskites oxidize and decompose above 550 °C, it would seem that hot isostatic pressing (HIP) in a controlled atmosphere is the only straightforward route to making dense ceramic samples.[17] There is one such example in the literature, in which Moroz *et al.* made

SrHfSe₃ pellets with 97% relative density by pressing at 850 °C and 100 MPa in a continuous argon gas flow.[16] This is an uncommon capability; and a more accessible sintering process, not requiring HIP equipment, will allow for more widespread studies on chalcogenide perovskite ceramics, such as the thermal and electronic transport measurements performed on sintered SrHfSe₃. [16] Additionally, dense material can be used as targets for thin film synthesis by pulsed laser deposition and sputtering.

The cold sintering process (CSP) can achieve high densification (> 90%) at sintering temperature below 300°C and pressure on the order of 100 MPa.[18] There is a long history of the development of this technique evolving from hydrothermal reaction and hydrothermal sintering methods, and it shares similarities to both.[19,20] What distinguishes CSP is that it is a wet sintering process in which the solvent is evaporated during densification. While the mechanisms that lead to densification in CSP are still debated, it is generally agreed that the addition of a liquid phase facilitates mass transport at low temperature (at least in some materials), leading to densification.[21,22] CSP has been shown to successfully densify a large range of materials, including ferroelectrics, microwave dielectrics, battery materials and semiconductors.[15,18,23–27] However, the focus has been almost exclusively on oxides. To date, the only published application of CSP to a chalcogenide has been on MoS₂/graphite composites.[15] In this work, ammonium molybdate tetrahydrate and thiourea were used instead of water as the liquid sintering aid, and 88% relative density was achieved by processing at 140 °C and 520 MPa for 60 mins. Attempts at CSP with water led to low relative density (~60%) due to the hydrophobic nature of MoS₂ and graphite.

The solvent most commonly used for CSP is water. However, water as a solvent for CSP of BaZrS₃ may be problematic. Studies on bulk materials and powder have shown good thermodynamic stability, but studies on thin films have shown degradation and surface oxidation in atmospheric conditions.[7,8,14,28] It can be expected that at the elevated temperature and pressure conditions of CSP, surface oxidation may be accelerated. For this reason, we study non-aqueous solvents for CSP of BaZrS₃. Non-aqueous solvents have been studied for CSP; for instance, dimethyl sulphoxide (DMSO) was used to eliminate secondary phase hydroxide precipitation during CSP of ZnO.[26,29]

Here we report on the densification of BaZrS₃ by sintering at low and intermediate temperatures (up to 500 °C) in non-aqueous solvents N,N-dimethylformamide (DMF), sulfur, and iodine. DMF and DMSO are commonly-used non-aqueous solvents, but unfortunately do not well dissolve ZnCl₄ or BaCl₂, which is indicative of whether a given solvent would aid in dissolution/precipitation reactions with BaZrS₃. BaCl₂ is known to lower the reaction temperature of BaZrS₃ solid state synthesis to 500 °C.[30] Using BaCl₂ as a solvent would be analogous to traditional liquid-phase sintering. However, since BaCl₂ cannot be removed during densification, unwanted impurities would be left behind. Excess sulfur was also shown to play a role in the reduction of solid-state reaction temperature, but only with BaCl₂ present.[28] The presence of sulfur during CSP could also aid in suppressing surface oxide formation. However, the high boiling point of sulfur (444 °C) requires temperatures that are above what is typical for CSP. Nonetheless, CSP with elemental sulfur as the additive may be worthwhile if using a temperature above the

boiling point. Iodine is another additive used in solid-state synthesis of chalcogenide perovskites, and as a transport agent in single-crystal growth.[31,32] Iodine melts at 114 °C and boils at 184 °C, and therefore is an attractive alternative to sulfur.

Results

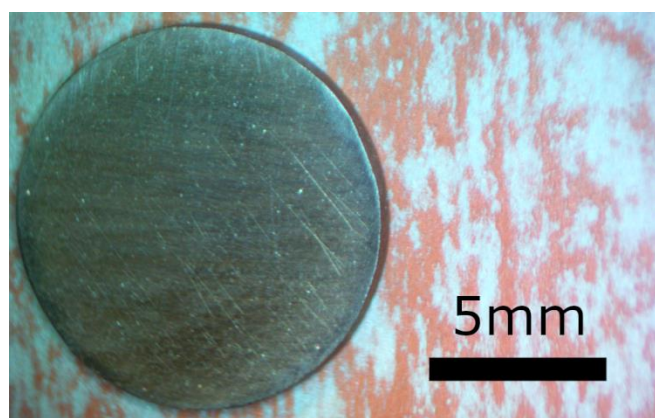


Figure 1: Sintered BaZrS₃ pellet (Sample O), and powder (reddish) removed during processing with sandpaper (light background).

Fig. 1 shows a BaZrS₃ pellet after CSP. The pellet was polished with 15,000 grit sandpaper, which appears as a blue background, against which the reddish BaZrS₃ powder is apparent. In **Table 1** we show the calculated density of fifteen pellets prepared with different sintering conditions. All samples exhibited low relative density (~80%), with the exception of CSP conditions at 450 °C and above with added iodine. CSP at 450 °C with 2 wt. % iodine added resulted in relative density of 92% (Sample C). A sample processed at the same conditions but with added sulfur instead of iodine (Sample B) did not achieve high densification, nor did the control sample sintered at 450 °C without additives (Sample D and F). **Fig. 2** shows scanning electron microscopy (SEM) micrographs of fracture surfaces of samples with 2 wt. % I₂ (Sample C) and 0 wt. % I₂ (Sample D). We see a much flatter fracture surface in the CSP sample with I₂. Both samples show nanometer-scale porosity. However, we also see larger pores in Sample D, which is consistent with its lower relative density. We also observe the presence of an unknown phase with glassy appearance in Sample C. Similar features were observed in Sample D, although to a much lesser extent. Further analysis of this phase would be required to determine its role in densification. We conclude from density and SEM measurements that added iodine contributes to densification through a mechanism involving enhanced mass transport, and not solely via accelerated compaction or creep, as these processes would also occur in the sample with added sulfur. Further analysis of the densification mechanism is made difficult by the fact the phase fraction of liquid iodine during processing is unknown due to its volatility, and that important chemical details of BaZrS₃ remain unknown, including its solubility in iodine and the nature of

defects at solid-liquid interfaces. As our understanding of chalcogenide perovskite materials and processing improves, then we may begin applying theoretical analysis developed for CSP.[33]

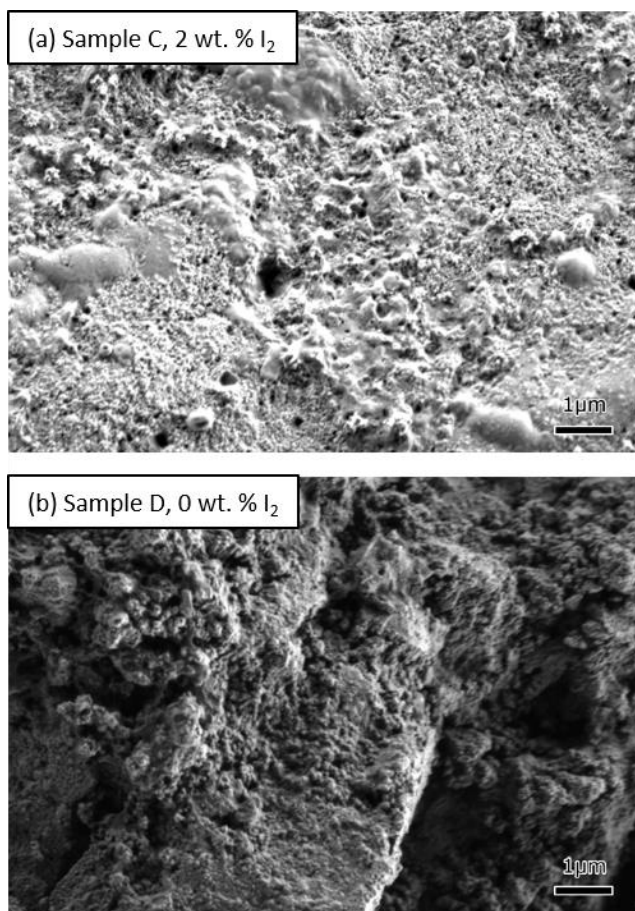


Figure 2: SEM micrographs of a CSP pellet fracture surfaces for samples processed (a) with 2 wt. % I₂ (Sample C), and (b) with 0 wt. % I₂ (Sample D).

Table 1: Summary of conditions used to sinter BaZrS₃. Density data are calculated from the geometric method, and particle sizes are estimated from a Scherrer analysis of XRD data; “bm” = ball-milled.

| Sample Label | Processing | Density (g/cm ³) | Relative Density | Particle Size (nm) |
|--------------|-----------------------------------|------------------------------|------------------|--------------------|
| A | As-synthesized powder | N/A | | |
| B | 450 °C, 10 wt. % S + 9 wt. % DMF | 3.44 ± 0.36 | 78% ± 8% | |
| C | 450 °C, 2 wt. % I ₂ bm | 4.05 ± 0.09 | 92% ± 2% | 37.7 +/- 19.2 |
| D | 450 °C control | 3.33 ± 0.08 | 76% ± 2% | 24.8 +/- 2.4 |
| E | As-synthesized powder | N/A | | 22.6 +/- 7.6 |
| F | 450 °C control | 3.46 ± 0.23 | 79% ± 5% | 17.5 +/- 8.8 |

| | | | | |
|---|--|-----------------|----------------|----------------|
| G | 230 °C, 9 wt. % DMF | 3.4 ± 0.07 | $78\% \pm 2\%$ | 18.0 ± 3.6 |
| H | 230 °C control | 3.37 ± 0.13 | $77\% \pm 3\%$ | 25.2 ± 5.1 |
| I | 230 °C, 5 wt. % I ₂ ground | 3.53 ± 0.07 | $80\% \pm 2\%$ | |
| J | 230 °C, 2 wt. % I ₂ ground | 3.48 ± 0.09 | $79\% \pm 2\%$ | |
| K | 230 °C, 1 wt. % I ₂ bm | 3.48 ± 0.07 | $79\% \pm 2\%$ | |
| M | 230 °C, 2 wt. % I ₂ bm | 3.5 ± 0.04 | $80\% \pm 1\%$ | 27.3 ± 9.9 |
| N | 230 °C, 5wt. % I ₂ ground | 3.39 ± 0.02 | $78\% \pm 1\%$ | |
| O | 500 °C, 2 wt. % I ₂ ground | 3.67 ± 0.03 | $84\% \pm 1\%$ | |
| P | 500 °C, 20 wt. % I ₂ ground | 3.97 ± 0.13 | $91\% \pm 3\%$ | |
| Q | 500 °C, 10 wt. % I ₂ ground | 4.00 ± 0.05 | $91\% \pm 1\%$ | |
| R | 500 °C control | 3.47 ± 0.10 | $79\% \pm 2\%$ | |

Since we observed densification with iodine at 450 °C, and the boiling point of iodine is 184 °C, we lowered the CSP reaction temperature to 230 °C (Samples G-N). We decided to remove the ball milling step for addition of iodine (I₂ bm) due to concerns that iodine may evaporate during this process, and to further simplify the technique. Instead, we mixed it in a mortar and pestle with BaZrS₃ (I₂ ground). We also explored variable I₂ loading, in the range of 1-5 wt. %. In CSP, it is common to see that increasing the wt. % of the liquid sintering aid increases final density up to a point, beyond which additional liquid sintering aid decreases the final density.[22] However, we observed no significant densification for any CSP samples processed at 230 °C compared to control samples without iodine (D, F and H), regardless of iodine wt. % or incorporation method. The hypothesis that iodine contributes to mass transport at higher temperature is further supported by the low density of pellets processed with iodine at 230 °C. If increased densification was only due to increased compaction from the added liquid, we would expect to see increased final density in the pellets processed at 230 °C.

We also made a series of samples at 500 °C (Samples O-R). Samples processed with 2 wt. % I₂ at 450 °C and 500 °C reached 92% (Sample C) and 84% (Sample O) relative density, respectively. At higher loadings of iodine, the relative density reached was 91% (Sample P, Q). It is unclear why higher loading of I₂ were required to reach similar densification as was achieved at 450 °C, though it could be due to fast evaporation of I₂ due to its high vapor pressure. Additionally, for Sample O, with 2 wt. % I₂, XRD revealed weak impurity peaks that matched some peaks from diffraction patterns for barium and zirconium iodide compounds, though phase identification was not possible. This leads us to believe that there are intergranular phases forming during the CSP process with iodine. Further work is required to uncover the densification mechanism that would explain these results.

Fig. 3a shows representative XRD data for as-synthesized BaZrS_3 powder (black curve), the starting material for sintering experiments. All peaks can be indexed to BaZrS_3 . We also show diffraction data measured after ball milling (red curve), and for Sample O after CSP (blue curve). We see a decrease in peak intensity and a broadening of peak widths attributed to reduction in particle size during ball milling. No additional peaks are visible in the ball-milled or CSP control sample D, processed without sintering aides. In CSP samples with iodine loading, additional impurity peaks were observed (**Fig. S2**). These impurities had weak intensities and could be matched to some compounds containing Ba, Zr, S, Fe, and I, but phase identification was not possible.

There is no indication of a change in particle size during CSP for processing temperature up to 500 °C. In **Fig. 3b** we present the data and Williamson-Hall models, and in **Fig. 3c** we present the inferred particle sizes. The particle sizes are in the range 20-30 nm, and we see no significant change between the ball-milled powders (Sample E) and any of the sintered samples. Optical microscopy of polished surfaces reveals apparent particle sizes larger than 100 μm (**Fig. S3**). It has been shown that a bimodal distribution of particles sizes can increase densification of BaTiO_3 by CSP.[34] It is unknown whether this effect is relevant here, or whether the larger particles observed in microscopy are coherent crystals. Nonetheless, diffraction data clearly show that ball-milled powders and sintered pellets are comprised primarily of small particles.

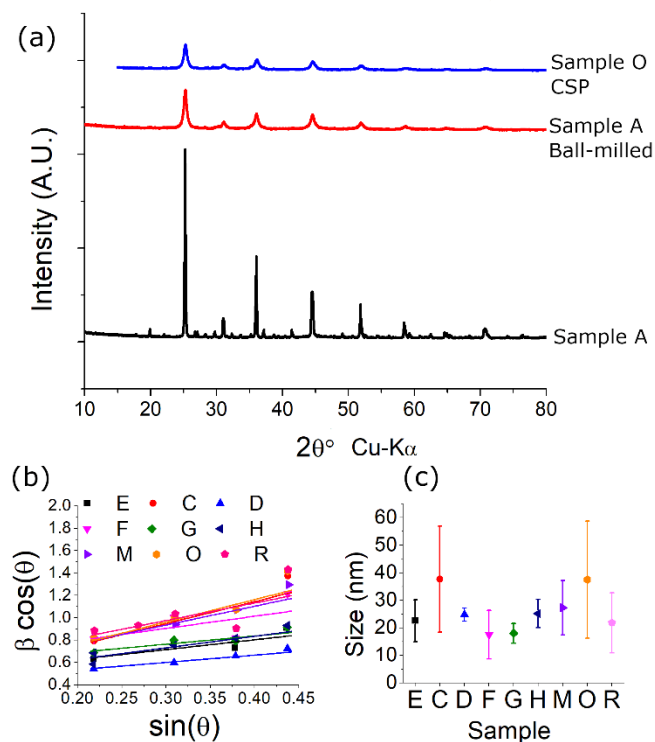


Figure 3: BaZrS_3 phase purity and particle size are unchanged by CSP processing with iodine (Sample O). (a) Powder diffraction of BaZrS_3 powder at different stages. (b) Williamson-hall fits, where β is the peak breadth. (c) Inferred average particle sizes.

Critical to the successful demonstration of chalcogenide perovskite CSP is to show that densification is possible in ambient conditions without any adverse effect on stoichiometry. The primary concern is sulfur loss and oxidation. We verified a 0.99:1 Ba:Zr ratio on pressed pellets with WDS. We estimated sulfur stoichiometry by measuring the mass change as a function of temperature. At high temperatures, above 550 °C, BaZrS₃ will decompose into BaSO₄ and ZrO₂.^[17,35,36] This decomposition reaction can be leveraged to calculate sulfur content from TGA data, as described above. In **Fig. 4** we show TGA data for as-synthesized powder, ball-milled powder and a control sample pressed with no additives (Sample R). We verified using XRD that the phase composition after reaching 1000 °C in the TGA is BaSO₄ and ZrO₂, with both monoclinic and tetragonal phases of ZrO₂ observed (**Fig. 4a**). The excess sulfur content for the starting powder was $x = 0.13$ (after Eqn. 1). This is consistent with TGA data on BaZrS₃ powder published previously by Niu *et al.*, which give $x = 0.15$, according to this same analysis.^[17] The oxygen content after ball milling was $y = 0.124 \pm 0.005$, and after CSP at 500 °C (Sample R) was $y = 0.128 \pm 0.001$. We conclude that a substantial quantity of oxygen is introduced during ball milling, but very little is further introduced during CSP. We take care during ball milling to minimize air exposure; however, since the powder size is greatly reduced by ball milling, it is unsurprising that the oxygen content would increase due to the increase in surface area. Meanwhile, further oxidation during CSP in ambient conditions is unlikely because BaZrS₃ is stable in air up to 550 °C.^[17]

Fig. 4b shows TGA data for CSP pellets processed with 0-20 wt. % I₂. Sample C (2 wt. % I₂) shows mass loss between 140 – 180 °C, which could be due to the evaporation of residual iodine. Further, gradual mass loss between 250 – 450 °C could be attributed to sulfur loss. However, the mass gain above 550 °C is significantly depressed, compared to a control sample without iodine. This effect is more pronounced in Sample P, with 20 wt. % I₂, for which mass loss continues above 450 °C and accelerates at 530 °C. Only above 700 °C do we again see mass gain consistent with oxidation into the final products, BaSO₄ and ZrO₂. Combined with XRD data only showing weak impurity peaks, we hypothesize that iodine is reacting to form unidentified iodide compounds in the intergranular regions. We note that decomposition products BaS (as opposed to BaSO₄) and ZrO₂ were reported in experiments processing Ba(Zr,Ti)S₃ in low-oxygen environments.^[37] However, since BaS is non-volatile, it is an unlikely candidate for the unknown compounds that form during TGA experiments on samples containing iodine

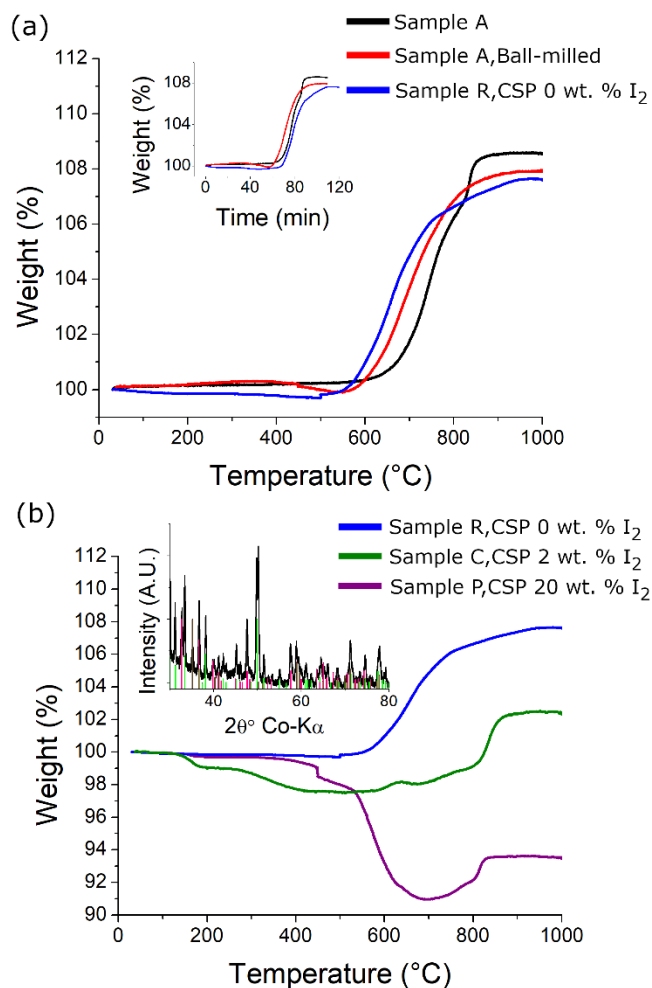


Figure 4: TGA data to quantify composition and illustrate the effect of added iodine. (a) Data for BaZrS₃ in different stages of processing (Samples A and R). Oxidation and decomposition above 500 °C results in mass gain. (Inset) Mass change as a function of time. (b) Data for CSP pellets (500 °C) with different iodine loadings (Samples R, C and P) showing that iodine reacts with BaZrS₃ to form unidentified compounds at high temperatures, likely in the intergranular regions. (Inset) XRD data confirming the final products as BaSO₄ and ZrO₂, heating up to 1000 °C in the TGA. Colored lines are marking the reflections from BaSO₄ (green lines) and ZrO₂ (pink and brown line for monoclinic and tetragonal phases respectively).

To understand the effect of CSP on the electrical properties of BaZrS₃, we measured the dielectric properties using impedance spectroscopy. In **Fig. 5** we present Nyquist plots of impedance data and corresponding models for samples processed 450 °C (Sample C) and 230 °C (Sample N). We fit the data for Sample N using a 2RQ circuit model (**Fig. 5**, inset). We observed a drift in time of the low-frequency response. Therefore, we only fit data above 1kHz, for which the data passes Kramer-Kronig validity testing.

The models yield high-frequency capacitance values of 59 ± 7 and 100 ± 30 pF for Samples C and N, respectively. Accounting for the geometric capacitance, we derive relative dielectric constants $\epsilon_{r,0} = 66 \pm 22$ and 116 ± 49 for Samples C and N respectively; a similar analysis yields $\epsilon_{r,0} = 104 \pm 72$ and 117 ± 62 for Samples O and Q. The uncertainties derive from error in fitting the high-frequency portion of impedance spectra, and from measurements of sample dimensions. These measurements of $\epsilon_{r,0}$ are consistent with our previously-reported single-crystal measurements, confirming that chalcogenide perovskites are the most highly-polarizable of known semiconductors with band gap in the VIS-NIR range (Fig. 6).[1] Although our measurements here suggest a higher $\epsilon_{r,0}$ than measured previously on single-crystal samples, the difference is not statistically significant. Extrinsic effects on the dielectric constant of pressed pellets are difficult to interpret because the nature of intergranular phases is unknown. Since our samples are highly resistive, consistent with low intrinsic doping, polarization and interface effects are not likely to contribute.

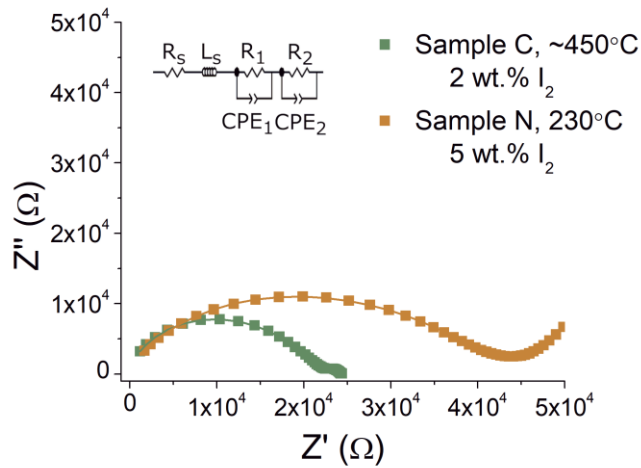


Figure 5: Impedance spectroscopy of BaZrS₃. Nyquist plots showing complex impedance data (points) and models (lines) for BaZrS₃ samples C and N sintered with iodine at 450 °C and 230 °C. The pellet processed at higher temperature has higher density and lower resistivity than the low-temperature, lower-density pellet; however, the inferred values for $\epsilon_{r,0}$ are comparable.

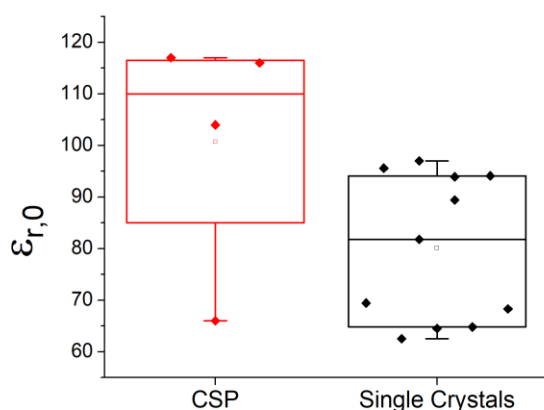


Figure 6: Relative low-frequency dielectric polarizability of BaZrS₃. Box-and-whisker plots summarize our measurements here on four CSP samples (left), and our previously-published measurements on single crystals (right).[1]

Conclusion

We have shown a technique for achieving high densification of BaZrS₃ powders at 450 °C and 425 MPa by adding ~2 wt. % of iodine. We show that this technique achieves high densification in short times (30 min) while not changing the powder grain size. Densification occurs in ambient atmosphere with no sample oxidation observed. Likewise, the bulk dielectric properties of the samples are unaffected. While this technique is inspired by the cold-sintering process, it is different because the sintering aid is not a liquid at room temperature. We hypothesize that iodine reacts to form an unidentified intergranular phase, leading to densification in BaZrS₃ pellets, as previously observed for CSP of BaTiO₃. [21]

The formation of intermediate, glassy phases is commonly reported in the literature on CSP.[21] Although CSP is cited as a low-temperature method, often CSP is followed by high-temperature annealing to fully crystallize material and improve properties. While this may seem paradoxical, CSP followed by a high-temperature firing step may still be simpler than alternative methods. It is possible that high-temperature sulfurization of BaZrS₃ CSP pellets containing iodine may lead to fully-dense BaZrS₃. Future work may also explore alternative solvents for chalcogenide perovskites, and for chalcogenide CSP more broadly. Thiourea-DMSO and amine-thiol solutions have been shown to dissolve Cu(In, Ga)(S, Se)₂ and Cu₂(Zn, Sn)(S, Se)₄. [38,39] A solvent that dissolves BaZrS₃ may enable densification at even lower temperature than reported here.

Methods

We made starting powders of BaZrS₃ via solid-state synthesis. We ground stoichiometric mixtures of BaS (Sigma-Aldrich, 99.9%) and ZrS₂ (Career Henan Chemical Co, 99.9%) with a mortar and pestle in a nitrogen glove box. We sealed the powders in a latex balloon and

isostatically cold-pressed them at 20 kpsi. We returned the resulting rod to the glove box and loaded it into a quartz ampule. We quickly transferred the ampules to a torch sealing apparatus, flushed with argon, and flame-sealed under 4 torr. We subsequently heated the ampules to 900 °C for 72 hours. We ground the resulting BaZrS₃ rod and dried it on a hot plate in a glove box at 480 °C to remove excess sulfur from the solid-state reaction. We sealed the resulting powder in a stainless-steel ball mill vial with stainless steel balls, working in a glovebox, and then milled the powders for two hours using a high-energy ball mill system at ambient conditions.

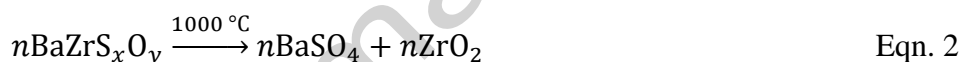
To prepare material for CSP, we mixed approximately 300 mg of BaZrS₃ powder with 1-10 wt. % of either anhydrous N,N-dimethylformamide (Sigma-Aldrich, 99.8%), sulfur (Sigma-Aldrich, 99.98%), or iodine (Sigma-Aldrich, 99.99%), working in a glove box. We additionally mixed samples with added sulfur and iodine using high-energy ball milling for 0.5 - 1 hr. We ground samples in a mortar and pestle to remove large agglomerations after ball milling, and then added DMF (if used). For each experiment, we loaded the mixture into a 10 mm-diameter, hardened-steel die, working in the glovebox. We transferred the die to a hot press (Carver) and then pressed it uniaxially under 425 MPa (7500 lbs) of pressure. We then increase the temperature to 230 ± 1 °C, 450 ± 20 °C, or 500 ± 20 °C, using a homemade heater jacket, and heated top and bottom plates of the press (**Fig. S1a-b**). When heating only with the press, we measured the temperature directly on the surface of the die. When using the heater jacket to reach temperatures above 300 °C, we used a thermocouple inserted into the fiberglass insulation to measure temperature. We found an uncertainty of ±20 °C depending on thermocouple placement and contact with die surface when using the heater jacket. We held the reaction temperature for 30 min before cooling to room temperature, all while maintaining the load at 425 MPa by manual adjustment. After sintering, we used sandpaper to grind and polish the samples, to remove surface contamination from the die, and to even the pellet thickness.

We measured bulk densities (ρ_b) for as-sintered pellets by using both caliper measurements of the pellet dimensions (geometric method) and using the Archimedes technique.[40] For Archimedes density measurements, we attached samples to a 1 mil thick plastic thread with glue (Elmers) and suspended in DMSO (assumed density of 1.1g/cm³). While the Archimedes method can be more accurate than caliper measurements, we found that for low density samples, liquid would get absorbed by the pellet, evidenced by bubble formation. This results in inflated estimates of the density. Therefore, we here report only density values calculated using the geometric method. For broken pellet pieces, sample area was calculated using image analysis software, ImageJ, and thickness was determined with caliper measurements. The theoretical density (ρ_{th}) for BaZrS₃ is 4.386 g cm⁻³. [41] The relative density was then calculated as ρ_b/ρ_{th} . A summary of samples and corresponding processing conditions can be found in **Table 1**.

We performed SEM experiments using a Zeiss Merlin high-resolution SEM; the images presented in **Fig. 2** were obtained using the secondary electron detector with an acceleration voltage of 1 kV and magnification of 10,050. We collected x-ray diffraction (XRD) patterns using Cu-K α radiation (PANalytical X'Pert PRO XRPD, operated at 45 kV and 40 mA). Diffraction patterns were collected at 2 θ angles between 10° and 80° with a step size of 0.026°, using bulk samples carefully polished with different grit papers (sizes #600, 1000, 1200, and 3000, 15000).

We used a Scherrer analysis to determine particle size after ball milling from XRD peak broadening. We calibrated our instrument for the Scherrer analysis with a LaB₆. We used a linear Williamson-Hall fit to estimate average particle size and strain. Peaks with low intensity or corresponding to impurities were excluded from the Williamson-Hall fit.

We measured the Ba:Zr ratio with wavelength-dispersive spectroscopy (WDS) in an electron microprobe (JEOL-JXA-8200 Superprobe). We used thermogravimetric measurements to calculate sulfur stoichiometry (TA Instruments Discovery TGA 7). We loaded ground powder samples in a platinum dish and heated to 1000 °C in air at 15 °C/min, with hold times at 200 °C for 15 min and at 1000 °C for 5 min. By the end of the 1000 °C hold, BaZrS₃ has decomposed into ZrO₂ and BaSO₄.^[17,35,36] We used XRD (Bruker D8 with a cobalt source and general area detector diffraction system (GADDS) and 0.5 mm collimator) to measure the powder after TGA experiments, to confirm the decomposition products. We calculated the sulfur content (*x* in Eqn. 1) for the as-synthesized powder samples by analyzing the mass change between the start of heating and when the decomposition-oxidation reaction was completed, as determined by flattening of the mass-time curve at high temperature. We then determine the amount of oxygen incorporated during ball milling and sintering (*y* in Eqn. 2) by repeating TGA experiments and analyzing the mass change using Eqn. 3, where MW is the molecular weight.



$$\text{MW}_{\text{before TGA}} = \frac{\text{starting mass}}{\text{final mass}} \times (\text{MW}_{\text{BaSO}_4} + \text{MW}_{\text{ZrO}_2}) \quad \text{Eqn. 3}$$

For impedance spectroscopy measurements, we made electrical contact to the polished sample surfaces with 80 nm-thick sputtered Au films. We then used Ag paint (Ted Pella Inc, PELCO colloidal silver #16031) to connect breakout wires to these contacts. The samples were then soldered into a test box with coaxial feedthroughs (**Fig. S1c**). We performed impedance spectroscopy measurements in ambient conditions over a frequency range, from 0.1 Hz to 1 MHz, using a Novocontrol Alpha-A impedance analyzer with a Pot/Gal 30V-2A Test Interface. We found that using Ag epoxy (CA-24, Bacon Adhesives) to connect wires instead of Ag paint left a residue that penetrated hundreds of microns into the samples, causing high sample resistance. For this reason, we do not present measurements on samples that were contacted with Ag epoxy.

Acknowledgments

We acknowledge support from the National Science Foundation (NSF) under grant no. 1751736, "CAREER: Fundamentals of Complex Chalcogenide Electronic Materials." A portion of this project was funded by the Skolkovo Institute of Science and Technology as part of the MIT-Skoltech Next Generation Program. This work was carried out in part through the use of the MIT Materials Research Laboratory (MIT MRL), MIT.nano, and the MIT Department of Materials Science shared experimental facilities.

Data Availability

The datasets generated during and/or analysed during the current study are available from the corresponding author on reasonable request.

Declarations

On behalf of all authors, the corresponding author states that there is no conflict of interest.

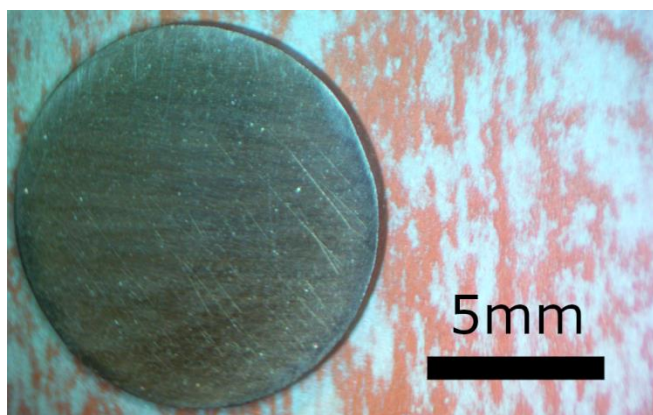
Accepted manuscript

References

- [1] Filippone S, Zhao B, Niu S, Koocher NZ, Silevitch D, Fina I, et al. Discovery of highly polarizable semiconductors BaZrS₃ and Ba₃Zr₂S₇. *Phys Rev Mater* 2020;4:091601. <https://doi.org/10.1103/PhysRevMaterials.4.091601>.
- [2] Jaramillo R, Ravichandran J. In praise and in search of highly-polarizable semiconductors: Technological promise and discovery strategies. *APL Mater* 2019;7:100902. <https://doi.org/10.1063/1.5124795>.
- [3] Nishigaki Y, Nagai T, Nishiwaki M, Aizawa T, Kozawa M, Hanzawa K, et al. Extraordinary Strong Band-Edge Absorption in Distorted Chalcogenide Perovskites. *Sol RRL* 2020;n/a:1900555. <https://doi.org/10.1002/solr.201900555>.
- [4] Sadeghi I, Ye K, Xu M, Li Y, LeBeau JM, Jaramillo R. Making BaZrS₃ Chalcogenide Perovskite Thin Films by Molecular Beam Epitaxy. *Adv Funct Mater* n.d.;n/a:2105563. <https://doi.org/10.1002/adfm.202105563>.
- [5] Sun Y-Y, Agiorgousis ML, Zhang P, Zhang S. Chalcogenide Perovskites for Photovoltaics. *Nano Lett* 2015;15:581–5. <https://doi.org/10.1021/nl504046x>.
- [6] Wei X, Hui H, Zhao C, Deng C, Han M, Yu Z, et al. Realization of BaZrS₃ chalcogenide perovskite thin films for optoelectronics. *Nano Energy* 2020;68:104317. <https://doi.org/10.1016/j.nanoen.2019.104317>.
- [7] Gupta T, Ghoshal D, Yoshimura A, Basu S, Chow PK, Lakhnot AS, et al. An Environmentally Stable and Lead-Free Chalcogenide Perovskite. *ArXiv191207082 Cond-Mat Physicsphysics* 2019.
- [8] Comparotto C, Davydova A, Ericson T, Riekehr L, Moro MV, Kubart T, et al. Chalcogenide Perovskite BaZrS₃: Thin Film Growth by Sputtering and Rapid Thermal Processing. *ACS Appl Energy Mater* 2020. <https://doi.org/10.1021/acsaem.9b02428>.
- [9] Pandey J, Ghoshal D, Dey D, Gupta T, Taraphder A, Koratkar N, et al. Local ferroelectric polarization in antiferroelectric chalcogenide perovskite BaZrS_3 thin films. *Phys Rev B* 2020;102:205308. <https://doi.org/10.1103/PhysRevB.102.205308>.
- [10] Shaili H, Beraich M, El Hat A, Ouafi M, Salmani EM, Essajai R, et al. Synthesis of the Sn-based CaSnS₃ chalcogenide perovskite thin film as a highly stable photoabsorber for optoelectronic applications. *J Alloys Compd* 2021;851:156790. <https://doi.org/10.1016/j.jallcom.2020.156790>.
- [11] Ravi VK, Yu SH, Rajput PK, Nayak C, Bhattacharyya D, Chung DS, et al. Colloidal BaZrS₃ chalcogenide perovskite nanocrystals for thin film device fabrication. *Nanoscale* 2021;13:1616–23. <https://doi.org/10.1039/D0NR08078K>.
- [12] Yu Z, Wei X, Zheng Y, Hui H, Bian M, Dhole S, et al. Chalcogenide perovskite BaZrS₃ thin-film electronic and optoelectronic devices by low temperature processing. *Nano Energy* 2021;85:105959. <https://doi.org/10.1016/j.nanoen.2021.105959>.
- [13] Márquez JA, Rusu M, Hempel H, Ahmet IY, Kölbach M, Simsek I, et al. BaZrS₃ Chalcogenide Perovskite Thin Films by H₂S Sulfurization of Oxide Precursors. *J Phys Chem Lett* 2021;12:2148–53. <https://doi.org/10.1021/acs.jpclett.1c00177>.
- [14] Perera S, Hui H, Zhao C, Xue H, Sun F, Deng C, et al. Chalcogenide perovskites – an emerging class of ionic semiconductors. *Nano Energy* 2016;22:129–35. <https://doi.org/10.1016/j.nanoen.2016.02.020>.

- [15] Nayir S, Waryoba DR, Rajagopalan R, Arslan C, Randall CA. Cold Sintering of a Covalently Bonded MoS₂/Graphite Composite as a High Capacity Li–Ion Electrode. *ChemNanoMat* 2018;4:1088–94. <https://doi.org/10.1002/cnma.201800342>.
- [16] Moroz NA, Bauer C, Williams L, Olvera A, Casamento J, Page AA, et al. Insights on the Synthesis, Crystal and Electronic Structures, and Optical and Thermoelectric Properties of Sr_{1-x}SbxHfSe₃ Orthorhombic Perovskite. *Inorg Chem* 2018;57:7402–11. <https://doi.org/10.1021/acs.inorgchem.8b01038>.
- [17] Niu S, Milam-Guerrero J, Zhou Y, Ye K, Zhao B, Melot BC, et al. Thermal stability study of transition metal perovskite sulfides. *J Mater Res* 2018;33:4135–43. <https://doi.org/10.1557/jmr.2018.419>.
- [18] Guo J, Guo H, Baker AL, Lanagan MT, Kupp ER, Messing GL, et al. Cold Sintering: A Paradigm Shift for Processing and Integration of Ceramics. *Angew Chem Int Ed* 2016;55:11457–61. <https://doi.org/10.1002/anie.201605443>.
- [19] Grasso S, Biesuz M, Zoli L, Taveri G, Duff AI, Ke D, et al. A review of cold sintering processes. *Adv Appl Ceram* 2020;119:115–43. <https://doi.org/10.1080/17436753.2019.1706825>.
- [20] Maria J-P, Kang X, Floyd RD, Dickey EC, Guo H, Guo J, et al. Cold sintering: Current status and prospects. *J Mater Res* 2017;32:3205–18. <https://doi.org/10.1557/jmr.2017.262>.
- [21] Guo H, Guo J, Baker A, Randall CA. Hydrothermal-Assisted Cold Sintering Process: A New Guidance for Low-Temperature Ceramic Sintering. *ACS Appl Mater Interfaces* 2016;8:20909–15. <https://doi.org/10.1021/acsami.6b07481>.
- [22] Kang X, Floyd R, Lowum S, Cabral M, Dickey E, Maria J-P. Mechanism studies of hydrothermal cold sintering of zinc oxide at near room temperature. *J Am Ceram Soc* 2019;102:4459–69. <https://doi.org/10.1111/jace.16340>.
- [23] Guo H, Baker A, Guo J, Randall CA. Cold Sintering Process: A Novel Technique for Low-Temperature Ceramic Processing of Ferroelectrics. *J Am Ceram Soc* 2016;99:3489–507. <https://doi.org/10.1111/jace.14554>.
- [24] Xin S, You Y, Wang S, Gao H-C, Yin Y-X, Guo Y-G. Solid-State Lithium Metal Batteries Promoted by Nanotechnology: Progress and Prospects. *ACS Energy Lett* 2017;2:1385–94. <https://doi.org/10.1021/acsenergylett.7b00175>.
- [25] Wang D, Tsuji K, Randall CA, Trolrier-McKinstry S. Model for the cold sintering of lead zirconate titanate ceramic composites. *J Am Ceram Soc* 2020;103:4894–902. <https://doi.org/10.1111/jace.17269>.
- [26] Kang X, Floyd R, Lowum S, Long D, Dickey E, Maria J-P. Cold sintering with dimethyl sulfoxide solutions for metal oxides. *J Mater Sci* 2019;54:7438–46. <https://doi.org/10.1007/s10853-019-03410-1>.
- [27] Sada T, Fan Z, Ndayishimiye A, Tsuji K, Bang SH, Fujioka Y, et al. In situ doping of BaTiO₃ and visualization of pressure solution in flux-assisted cold sintering. *J Am Ceram Soc* 2021;104:96–104. <https://doi.org/10.1111/jace.17461>.
- [28] Wang Y, Sato N, Yamada K, Fujino T. Synthesis of BaZrS₃ in the presence of excess sulfur. *J Alloys Compd* 2000;311:214–23. [https://doi.org/10.1016/S0925-8388\(00\)01134-8](https://doi.org/10.1016/S0925-8388(00)01134-8).
- [29] Seo J-H, Nakaya H, Takeuchi Y, Fan Z, Hikosaka H, Rajagopalan R, et al. Broad temperature dependence, high conductivity, and structure-property relations of cold sintering of LLZO-based composite electrolytes. *J Eur Ceram Soc* 2020;40:6241–8. <https://doi.org/10.1016/j.jeurceramsoc.2020.06.050>.

- [30] Wang Y, Sato N, Fujino T. Synthesis of BaZrS₃ by short time reaction at lower temperatures. *J Alloys Compd* 2001;327:104–12. [https://doi.org/10.1016/S0925-8388\(01\)01553-5](https://doi.org/10.1016/S0925-8388(01)01553-5).
- [31] Niu S, Huyan H, Liu Y, Yeung M, Ye K, Blankemeier L, et al. Bandgap Control via Structural and Chemical Tuning of Transition Metal Perovskite Chalcogenides. *Adv Mater* 2017;29:1604733. <https://doi.org/10.1002/adma.201604733>.
- [32] Niu S, Sarkar D, Williams K, Zhou Y, Li Y, Bianco E, et al. Optimal Bandgap in a 2D Ruddlesden–Popper Perovskite Chalcogenide for Single-Junction Solar Cells. *Chem Mater* 2018;30:4882–6. <https://doi.org/10.1021/acs.chemmater.8b01707>.
- [33] Biesuz M, Taveri G, Duff AI, Olevsky E, Zhu D, Hu C, et al. A theoretical analysis of cold sintering. *Adv Appl Ceram* 2020;119:75–89. <https://doi.org/10.1080/17436753.2019.1692173>.
- [34] Guo H, Baker A, Guo J, Randall CA. Protocol for Ultralow-Temperature Ceramic Sintering: An Integration of Nanotechnology and the Cold Sintering Process. *ACS Nano* 2016;10:10606–14. <https://doi.org/10.1021/acsnano.6b03800>.
- [35] Yan J, Greenblatt M, Sahiner A, Sills D, Croft M. Ruddlesden–Popper zirconium sulfides—a novel preparation method and characterization of electronic structure. *J Alloys Compd* 1995;229:216–22. [https://doi.org/10.1016/0925-8388\(95\)01678-3](https://doi.org/10.1016/0925-8388(95)01678-3).
- [36] Nitta T, Nagase K, Hayakawa S. Formation, Microstructure, and Properties of Barium Zirconium Sulfide Ceramics. *J Am Ceram Soc* 1970;53:601–4. <https://doi.org/10.1111/j.1151-2916.1970.tb15981.x>.
- [37] Wei X, Hui H, Perera S, Sheng A, Watson DF, Sun Y-Y, et al. Ti-Alloying of BaZrS₃ Chalcogenide Perovskite for Photovoltaics. *ACS Omega* 2020;5:18579–83. <https://doi.org/10.1021/acsomega.0c00740>.
- [38] Li W, Tan JMR, Leow SW, Lie S, Magdassi S, Wong LH. Recent Progress in Solution-Processed Copper-Chalcogenide Thin-Film Solar Cells. *Energy Technol* 2018;6:46–59. <https://doi.org/10.1002/ente.201700734>.
- [39] Zhao X, Zhang R, Handwerker C, Agrawal R. The potential of amine-thiol based solution processing for chalcogenide photovoltaics. 2016 IEEE 43rd Photovolt. Spec. Conf. PVSC, 2016, p. 0542–4. <https://doi.org/10.1109/PVSC.2016.7749653>.
- [40] Hughes SW. Archimedes revisited: a faster, better, cheaper method of accurately measuring the volume of small objects. *Phys Educ* 2005;40:468–74. <https://doi.org/10.1088/0031-9120/40/5/008>.
- [41] Niu S, Zhao B, Ye K, Bianco E, Zhou J, McConney ME, et al. Crystal growth and structural analysis of perovskite chalcogenide BaZrS₃ and Ruddlesden–Popper phase Ba₃Zr₂S₇. *J Mater Res* 2019;34:3819–26. <https://doi.org/10.1557/jmr.2019.348>.



Accepted manuscript